Selective Angular Momentum Generator Based on a Graphene Hybrid Plasmonic Waveguide

Feng Chao Ni, Ze Tao Xie , Xi-duo Hu, Chuan-yu Jia, and Xu Guang Huang

Abstract—Manipulation of the angular momentum (AM) of photons is of great importance in many fields such as optical communications, holographic, and particle manipulation. Although there are many demonstrations focusing on dynamic manipulation of AM in free space, the active tuning of AM in nanophotonic waveguides is mainly exclusive, especially in the Terahertz regime. Here we propose a selected AM generation scheme based on graphene hybrid waveguide, which can convert a quasi-linear mode into a quasi-circular mode with dynamic tuning manner. Also, we show that the proposed waveguide structure can serve as a distinguisher between left- and right-handed quasi-circular modes. These results allow for the dynamic control of AM of light in nanophotonic waveguides, which are crucial for various devices with compact footprint, such as on-chip biosensing and integrated quantum information processing.

Index Terms—Angular momentum, birefringence effect, graphene surface plasmons, hybrid waveguide.

I. INTRODUCTION

PLASMONIC waveguides/structures consist of a metal or metalloid (like graphene) and one or several dielectrics with strong light confinement. They have been extensively investigated for numerous applications such as resonator [1], bend [2], beam splitter [3], filter [4], modulator and variable optical attenuator [5].

Angular momentum (AM) of photons can be decomposed into two independent terms: spin angular momentum (SAM) and orbital angular momentum (OAM). SAM is related to the polarization state of photons: $+\hbar$ for a left-handed circularly polarized mode and $-\hbar$ for a right-handed circularly polarized

F. C. Ni and Z. T. Xie are with the Guangdong Provincial Key Laboratory of Nanophotonic Functional Materials and Devices, School of Information and Optoelectronic Science and Engineering, South China Normal University, Guangzhou 510006, China (e-mail: nfc456@foxmail.com; 874361223@qq.com).

X. Hu and C. Jia are with the School of Electronic Engineering, Dongguan University of Technology, Dongguan 523808, China (e-mail: 527090411@qq.com; cyjia04040@sina.com).

X. G. Huang is with the Guangdong Provincial Key Laboratory of Nanophotonic Functional Materials and Devices, Guangzhou Key Laboratory for Special Fiber Photonic Devices and Applications, South China Normal University, Guangzhou 510006, China (e-mail: huangxg@scnu.edu.cn).

Color versions of one or more of the figures in this article are available online at http://ieeexplore.ieee.org.

Digital Object Identifier 10.1109/JLT.2019.2941837

mode [6]. Light beams possessing SAM have been widely used in quantum information processing [7], photon spin hall effect [8], optical communication [9], [10], chirality distinguishing [11] and imaging [12], [13]. In addition, OAM is related to a spiral phase front [14], [15], a beam with helical wavefront carries OAM of $\ell\hbar$ per photon, where ℓ is the topological charge. Also, OAM is essential for optical communication [16], multiplexing [17] and quantum information technology [18].

Various methods have been proposed to generate SAM/OAM beams. The SAM beams are traditionally created by using quarter-wave plates (QWPs). The first method is to use a birefringent crystal [19]. Birefringence is the physical phenomenon where an incident light is decomposed into two beams of light refracted in different directions in an anisotropic crystal, which has many applications such as photonic crystal fibers [20], [21], [22], [23]. However, birefringent crystals are difficult to achieve high integration because of their relatively large sizes. Secondly, metasurface-based QWPs provide a new way to address the integrated challenge [24], [25]. However, there are still several issues, such as a narrow operation band [26], complexity in fabrication [27] and only working in free space. The third choice is using nanophotonic waveguide with ultra-compact structure, low loss and wide operation bandwidth [28], which may be a promising choice for the manufacture of on-chip QWPs. As for OAM beams, there are various methods for creating and manipulating OAM beams, such as computing holography [29], spiral phase plates [30], cylindrical lens mode converters [31] and Q-plates [32]. The common disadvantages to all of these methods are the large size and the mechanical complexity, which will restrict their on-chip integration.

There are several reports in the academic community about optical devices that generate both SAM and OAM. Optical devices such as Q-plates [33], [34] and fibers [35], [36] can generate light beams carrying both SAM and OAM. However, due to their large size, it is not conducive to the on-chip integration of the devices. Metasurfaces can also be used to manipulate the generation and coupling of SAM and OAM [37], [38], but they can only work in free space, rather than waveguides. Another method is based on the waveguide structure of silicon-on-insulator (SOI) platform [39], [40], but the operating frequency bands of these structures are still unable to reach Terahertz regime and have poor tunability. Terahertz technology has been applied in various fields, such as ultra-fast wireless communication, imaging, environmental monitoring and other fields. 100 μm ($\sim$3 THz) is a typical wavelength in Terahertz range for scientific, military, and commercial applications [41].

There are many studies work on the wavelength of 100 μm, such as quantum-cascade laser [42] and ultralow loss waveguide [43].

Graphene, an important carbon nanomaterial (CNM), is a 2D monolayer of carbon atom arranged in a honeycomb lattice [44], [45]. It has been theoretically [46] and experimentally [47] proved that it can excite surface plasmons (SPs), which has aroused widespread concern in science community. Compared with metal surface plasmons (MSPs), the Fermi level of the graphene can be dynamically adjusted by controlling gate voltage or chemical doping [48], [49]. Moreover, the optical field of graphene surface plasmons (GSPs) can be confined down to volumes that are smaller than MSPs. The advent of graphene has created a broader platform for the study of surface plasma optics.

In this work, for the first time to our knowledge, we propose a graphene hybrid plasmonic waveguide (GHPW) that can manipulate the AM of photons in the Terahertz regime, the birefringence of the GHPW is used to convert a quasi-linearly polarized mode to a quasi-circularly polarized mode with a longitudinal OAM mode. Moreover, by changing the Fermi level of graphene, we can dynamically adjust the polarization state of the light beams.

II. DESIGN OF GRAPHENE HYBRID PLASMONIC WAVEGUIDE

In Terahertz regime, graphene can be regarded as an infinitesimally thin conductive layer. Compared with propagation characteristics of GSPs of monolayer graphene, few-layer graphene SPs have the ability to effectively reduce the number of SP wavenumber [50], which lead to a weaker confinement to SP mode and smaller propagation loss. Therefore, in our work, a few-layer graphene sheet is used to construct the GHPW.

Under the condition of random phase approximation, the surface conductivity σ_g of a monolayer graphene can be written according to Kubo formula [51]:

$$
\begin{aligned}
\sigma_g(\omega, \tau, T, E_f) = & \frac{2ie^2 k_B \mathrm{T}}{\pi \hbar^2 (\omega + i\tau^{-1})} \ln\left[2\cosh\left(\frac{E_f}{2k_B T}\right)\right] \\
& + \frac{e^2}{4\hbar}\left\{\frac{1}{2} + \frac{1}{\pi}\arctan\left(\frac{\hbar\omega - 2E_f}{2k_B T}\right)\right. \\
& \left. - \frac{i}{2\pi}\ln\left[\frac{(\hbar\omega + 2E_f)^2}{(\hbar\omega - 2E_f)^2 + (2k_B T)^2}\right]\right\},
\end{aligned}
$$

here $\hbar$ is reduced Planck's constant, ω the radian frequency, k_B the Boltzmann constant, $T = 300$ K the room temperature, $\tau = 0.5$ ps the carrier relaxation time. The Fermi level of graphene can be calculated by $E_f = \hbar v_f (\pi n_g)^{1/2}$ (where v_f is Fermi velocity, n_g is carrier concentration). It should be noted that the graphene with the Fermi level of 0.9 eV has been achieved [52]. Hence, the Fermi level of graphene is set from 0.2 eV to 0.9 eV in this study. A few-layer graphene can be regarded as a stack of several of non-interacting monolayer graphene, its optical conductivity can be expressed as $N\sigma_g$ (where N is the number of layers, $N < 6$) [53]. In addition, for a few-layer graphene with $N < 6$, its absorption loss decreases as the number
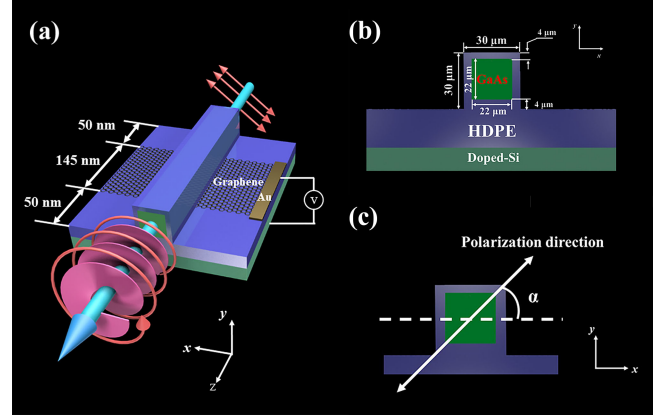

Fig. 1. (a) Schematic of the proposed GHPW: a quasi-linearly polarized mode converts into a transverse quasi-circularly polarized mode (E_T) with a longitudinal OAM mode (E_Z); (b) Cross section of the GHPW; (c) Definition of the polarization angle α of the quasi-linearly polarized mode.

of layers increases. Therefore, to reduce the propagation loss of the GSPs, the number of layers is fixed at $N = 5$. In this paper, we numerically analyze the GHPW by using the finite difference time domain method (FDTD) [54] in the commercial software of Lumerical FDTD Solutions [55]. In the simulation domain, the grid sizes of Δx, Δy and Δz in transverse directions (x- and y-coordinates) and longitudinal direction (z-coordinate) are all 0.5 μm, and the dimensions of the whole simulation domain are $[x, y, z] = [60\,\mu\text{m}, 60\,\mu\text{m}, 300\,\mu\text{m}]$. In addition, perfectly matching layer (PML) absorbing boundary conditions are applied in all directions. The 2D conductivity model described is used to simulate the optical properties of graphene, and the effective indices of different waveguide section are calculated using the mode solver simulation in the FDTD Solutions.

Fig. 1(a) present the function of the proposed GHPW, which can convert a linearly polarized Terahertz beam to an AM light beam, with transverse SAM mode and longitudinal OAM mode. Fig. 1(b) shows the construction and the geometry of waveguide cross section. The GHPW consists of three parts, the high-index (3.6) dielectric core of the first and third sections is gallium arsenide (GaAs), which surrounded by low-index (1.54) dielectric cladding of high-density polyethylene (HDPE), both GaAs and HDPE have been widely employed in Terahertz regime [56], [57]. The second part is a hybrid waveguide, where the AM light beam is generated. In this part, the graphene is underneath the HDPE under-cladding of the dielectric waveguide, the thickness of the HDPE layer sandwiched between square GaAs waveguide and five-layer graphene is 4 μm. A gold (Au) electrode and a doped-silicon (Doped-Si) substrate are located on the top of graphene and the below of the HDPE layer, respectively. When coupled into the GHPW, the quasi-linearly polarized light must propagate a certain transmission distance to form a relatively stable mode field distribution. Therefore, the length of the first section of GHPW is fixed at 50 μm. Similarly, the length of the third section is also set to 50 μm. And the operating wavelength is $\lambda = 100\,\mu$m.

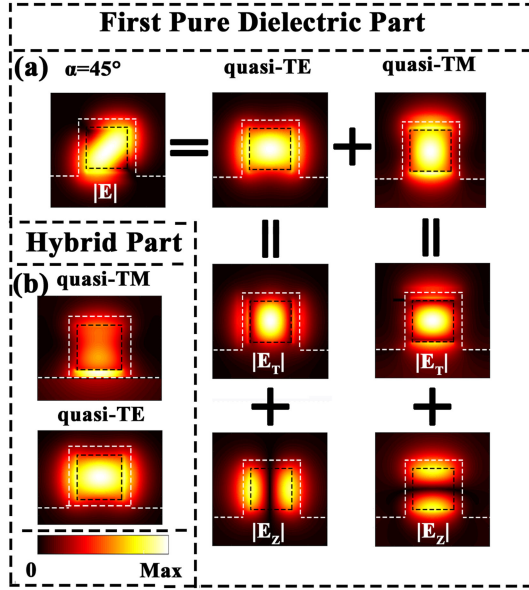A possible fabrication scheme for the hybrid waveguide could be as follows: (1) Spin coating a HDPE layer on doped silicon

Fig. 2. (a) In the first pure dielectric part of GHPW, the amplitude distribution of a quasi-linearly polarized light with $\alpha = 45°$, which can be decomposed into a quasi-TE mode and a quasi-TM mode. E_T and E_Z represent the transverse and he longitudinal electric field component of the two modes, respectively; (b) The amplitude distributions of the quasi-TE mode and the quasi-TM mode in the second part of waveguide.

substrate, and then covering graphene sheet on the HDPE layer; (2) spin coating a HDPE layer on graphene sheet to form HDPE under-cladding; (3) the process of molecular beam epitaxy (MBE) [58], and following up photolithograph with reactive ion etching (RIE) [59], to form the GaAs core; (4) spin coating, photolithograph and RIE onto a HDPE to form HDPE thin film covering the top and sidewalls of the GaAs core; (5) making gold electrode pads for gate voltage.

III. BIREFRINGENCE EFFECT OF THE GRAPHENE HYBRID PLASMONIC WAVEGUIDE

The proposed GHPW exhibits a huge birefringence effect, the quasi-TE mode and the quasi-TM mode will present a large difference of amplitude distribution in the hybrid part. Hence, we use this characteristic to "spin" and "twist" photons. In the first pure dielectric part, a quasi-linearly polarized light with $\alpha = 45°$ can be decomposed into a quasi-TE mode and a quasi-TM mode with equal amplitude, as shown in Fig. 2(a). Both modes can be decomposed into a transverse electric field component E_T and a longitudinal electric field component E_Z. Since the waveguide has a strong transversal confinement, the electric field in the waveguide is no longer just a transverse electric field E_T, and will generate a longitudinal electric field component E_Z pointing in the direction of light propagation. The relationship between the E_T and E_Z can be expressed as [60]:

$$E_Z = \frac{1}{i\beta}\nabla_T E_T, \qquad (2)$$

where β is a propagation constant, and ∇_T is the transverse gradient. The amplitude of the E_Z can be adjusted by changing

the geometric parameters of the waveguide, which can be as high as 97% of the amplitude of the E_T [61]. In addition, the 0th order modes at the center of the GaAs square waveguide are purely transversal, while the amplitude of the longitudinal component E_Z equals 0, and for the light beam with $\lambda = 100\,\mu m$, high-order modes are suppressed and cannot be stably exist in the proposed waveguide. Thus, we use the polarization state at the central point of waveguide to represent the polarization state of the transverse component E_T. The polarization angle α of the incident light can be defined as:

$$\tan(\alpha) = \left| \frac{E_{T-TMl}}{E_{T-TEl}} \right|, \qquad (3)$$

here, $|E_{T-TMl}|$ and $|E_{T-TEl}|$ represent the amplitudes of the transverse component of the quasi-TM mode and the quasi-TE mode in the first part of waveguide, respectively. In the first part, the effective indices of the quasi-TE mode and the quasi-TM mode are nearly equal, about 2.45. However, when the light beam transmits to the hybrid part of the waveguide with $E_f = 0.9\,eV$, the mode field distributions of the two modes are greatly different, as shown in Fig. 2(b). The real-part difference of effective index between the two modes can be expressed as:

$$\Delta n = Re\left[n_{quasi-TM} - n_{quasi-TE}\right], \qquad (4)$$

where $n_{quasi-TM} = 2.568 + 0.0025i$ and $n_{quasi-TE} = 2.397 + 0.0021i$ are the effective indices of the quasi-TM mode and -TM mode in the hybrid part of GHPW, respectively. The imaginary part of the effective indices between the two modes, which characterize the propagation loss of two modes, can be negligible for their small difference. In this case, the real-part difference of effective index is calculated to be $\Delta n = 0.171$, which will affect the phase shift δ between two modes. The relative phase can be expressed as:

$$\delta = k_0 \Delta n L_g + \Delta\delta \qquad (5)$$

Where $k_0 = 2\pi/\lambda$ is the free space wave vector, L_g is the length of the five-layer graphene sheet, and $\Delta\delta$ is the relative phase caused by other factors. Assuming that $\Delta\delta = 0$ and $\lambda = 100\,\mu m$, the theoretical length of the graphene is calculated to be $L_g = 146.2\,\mu m$ for the requirement of $\delta = \pi/2$. We use the 3D FDTD method to verify our conclusion. As seen in Fig. 3, as the length of the graphene length L_g increases, the relative phase δ between the quasi-TM mode and -TE mode increases, and the data calculated by FDTD is very close to the result obtained by eq. (5). When the simulated relative phase δ is $\pi/2$, the graphene length L_g is set as 145 μm, which is approximately equal to the theoretical length of graphene calculated by eq. (5).

IV. TRANSVERSE ELECTRIC FIELD COMPONENT AND POLARIZATION STATE

As we all known, the polarization state of light beam can be described by the amplitude ratio $\tan(\Phi)$ and the relative phase δ between transverse electric field components E_T of the quasi-TM mode and the quasi-TE mode. In the third pure dielectric
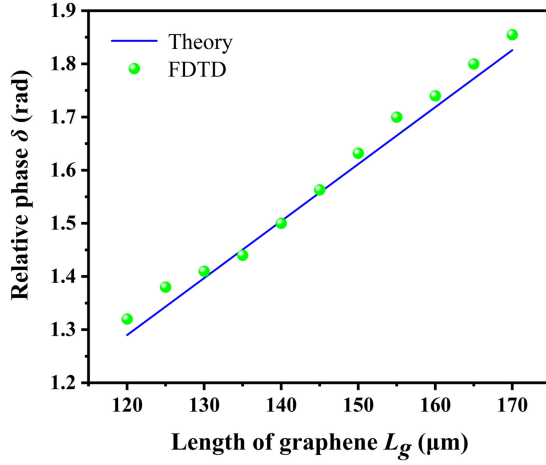
Fig. 3. The theoretical and FDTD simulated result of the relative phase δ in the GHPW structure.

part of GHPW, $\tan(\Phi)$ can be expressed as:

$$\tan \Phi = \frac{|E_{\text{T}-\text{TM3}}|}{|E_{\text{T}-\text{TE3}}|} = \frac{k_1}{k_2} \frac{|E_{\text{T}-\text{TM1}}|}{|E_{\text{T}-\text{TE1}}|} = \frac{k_1}{k_2} \tan \alpha, \quad (6)$$

where $|E_{\text{T}-\text{TM3}}|$ and $|E_{\text{T}-\text{TE3}}|$ represent the amplitudes of the transverse component of the quasi-TM mode and the quasi-TE mode in the third part of waveguide, k_1 and k_2 are the propagation constant related to the propagation loss of the two modes in the waveguide. According to eqs. (5) and (6), we can change the polarization state in the third part by changing the polarization angle of the incident light and the length of the graphene. For $\alpha = 45°$, the quasi-linearly polarized light will be converted into a left-handed circularly polarization light, assuming that $L_g = 145\,\mu m$ and $E_f = 0.9\,\text{eV}$. For $\alpha = -45°$, the quasi-linearly polarized light will be converted into a right-handed circularly polarization light. Thus, by manipulating the $\pm$ signs of the initial polarization direction angle α, we can manipulate the spin state of the emitted photons.

V. LONGITUDINAL ELECTRIC FIELD COMPONENT AND VORTEX BEAM

According to the previous discussion, we know that after passing through the hybrid part of the proposed GHPW, the output light of the third part is not conventional elliptically polarized light because there is a longitudinal electric field component E_Z in the waveguide. In this work, we found that while the transverse electric field component E_T carries the SAM, the longitudinal electric field component E_Z will simultaneously carry the OAM with the spiral phase. Eq. (2) reveals that there is a fixed phase difference of $\pi/2$ between the E_Z and the E_T, which means that there is a case where the spin direction of the light field is perpendicular to the direction of light propagation in the waveguide. Thus, the longitudinal components E_Z of the quasi-TM mode and the quasi-TE mode exist the same relative phase difference δ. Fig. 4(a) and (b) show the amplitude distribution of E_Z components in the first and third waveguide parts. In the first waveguide part, the relative phase
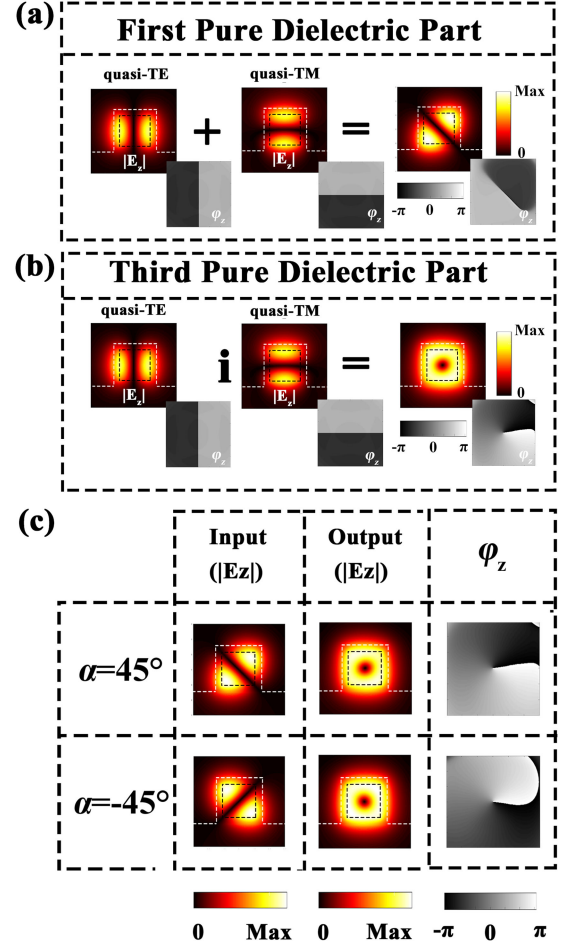

Fig. 4. The field and phase distributions of the longitudinal component E_Z of the quasi-TE mode and the quasi-TM mode superimposed in the (a) first and (b) third pure dielectric part of the waveguide, respectively; (c) The field and phase distributions of E_Z for $\alpha = 45°$ and $\alpha = -45°$ in the third pure dielectric part of the waveguide.

difference between the quasi-TM mode and the quasi-TE mode is 0, thus, the superposition field of the E_Z components of the two modes present an antisymmetric field distribution. After passing through the hybrid waveguide part, the E_Z component of output light beam results in a vortex carrying OAM, which is generated by the birefringence effect of the GHPW. The electric field of a vortex light beam can be expressed as:

$$E_Z(r, \theta) = A(r)e^{i\ell\theta}, \quad (7)$$

where r and θ are polar coordinate parameters, $A(r)$ is the amplitude of the electric filed, and ℓ is the topological charge. The $\pm$ signs of polarization angle α not only affect the handedness of the transverse electric field component E_T, but also affect the handedness of the vortex of the longitudinal component E_Z. As shown in Fig. 4(c), assuming that $L_g = 145\,\mu m$ and $E_f = 0.9\,\text{eV}$, for $\alpha = 45°$, the spiral phase of the vortex beam rotates counterclockwise ($\ell = 1$); for $\alpha = 45°$, the spiral phase rotates clockwise ($\ell = -1$).
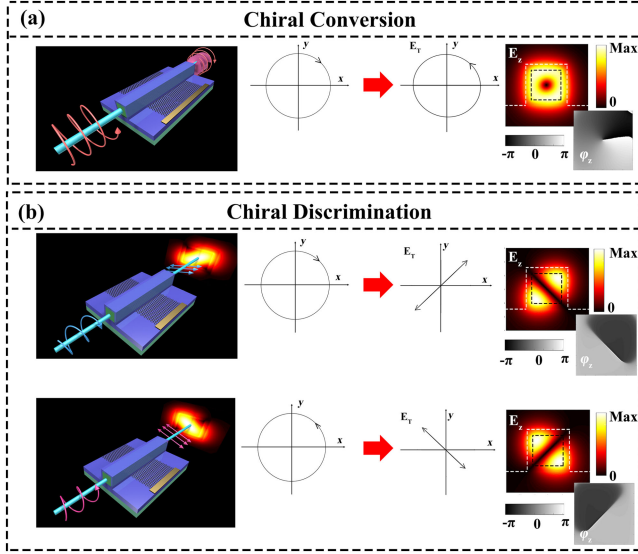
Fig. 5. (a) Schematic of chiral converter: a right-handed polarized light is converted into a left-handed quasi-circularly polarized light carrying OAM component E_Z with spinning- counterclockwise spiral phase; (b) Schematic of chiral discriminator: a quasi-linearly polarized output light with $\alpha = -45°$ for the left-handed circularly polarized light, and $\alpha = 45°$ for the right-handed circularly polarized light.

VI. CHIRAL CONVERSION AND CHIRAL DISCRIMINATION

We have demonstrated the scheme for converting a quasi-linearly polarized mode with $\alpha = 45°$ into a quasi-circularly polarized light. However, in many fields, such as integrated quantum computing, on-chip biosensing, terahertz communication, etc., it is expected that chiral conversion and chiral discrimination can be realized on a chip without resorting to bulk devices to achieve this function. From the previous discussion, we know that the relative phase δ between the quasi-TM mode and the quasi-TE mode depends on the length of the graphene L_g in the hybrid waveguide part. By doubling the length of graphene, a half-wave plate can be obtained, which can achieve the function of chiral conversion. While the length of graphene increased to 290 μm with $E_f = 0.9\,\text{eV}$, according to eq. (5), the relative phase δ is π, Fig. 5(a) shows the function of chiral conversion of the GHPW. Similarly, while the length of graphene is 145 μm, the relative phase is $\pi/2$. In this case, a quasi-linearly polarized output light with $\alpha = -45°$ for the left-handed circularly polarized light, and $\alpha = 45°$ for the right-handed circularly polarized light, as shown in Fig. 5(b). Therefore, the function of chiral discrimination can be realized by distinguishing the polarization angle of the emitted linearly polarized light. In addition, the conversion of quasi-linearly polarized light with $\alpha = 45°$ to right-handed quasi-circularly polarized light can be achieved while the length of graphene increased to 435 μm.

VII. DYNAMIC TUNABILITY OF THE GRAPHENE HYBRID PLASMONIC WAVEGUIDE

The Fermi level E_f of graphene can be dynamically adjusted by controlling gate voltage. The change of Fermi level will cause the effective indices of the quasi-TE mode and the quasi-TM
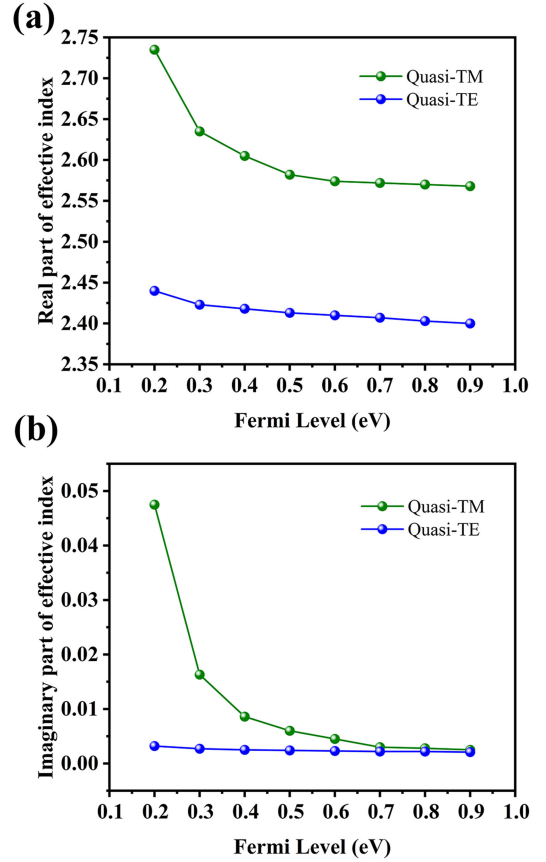

Fig. 6. The dependences of the (a) real and (b) imaginary parts of the effective indices on the graphene Fermi level in the hybrid waveguide part for the quasi-TM mode and the quasi-TE mode.

mode in the hybrid part to change. To illustrate this point, we simulate a case that the graphene Fermi level changed from 0.9 eV to 0.2 eV, with $\lambda = 100\ \mu$m, $L_g = 145\ \mu$m and $\alpha = 45°$. As shown in Fig. 6, it can be clearly seen that as the Fermi level decreases, the real part and the imaginary part difference of effective indices between the two modes gradually increases. According to eqs. (5) and (6), the relative phase δ and the amplitude ratio $\tan(\Phi)$ of the E_T components of the two modes, are functions of Fermi level E_f. When E_f drops from 0.9 eV to 0.2 eV, the relative phase δ rises from 1.57 to 2.56, while the amplitude ratio $\tan(\Phi)$ decreases from 0.96 to 0.214. As mentioned above, the transverse component E_T and the longitudinal component E_Z in the waveguide are related, which means that the polarization state of E_T and the distribution of E_Z are interrelated. When one adjusts the Fermi level of graphene, it not only varies the polarization state polarization state of the transverse component E_T and the distribution of the longitudinal component E_Z of the output light, but also changes the propagation loss of the waveguide. Fig. 7 shows the polarization state of the transverse component E_T of the output beam and the field distribution of the OAM component E_Z when the Fermi level is 0.2 eV, 0.4 eV, and 0.9 eV, respectively. Fig. 8 shows the propagation loss (which is defined as $|10\lg T|$, T is the transmittance of the GHPW) of the waveguide versus the Fermi
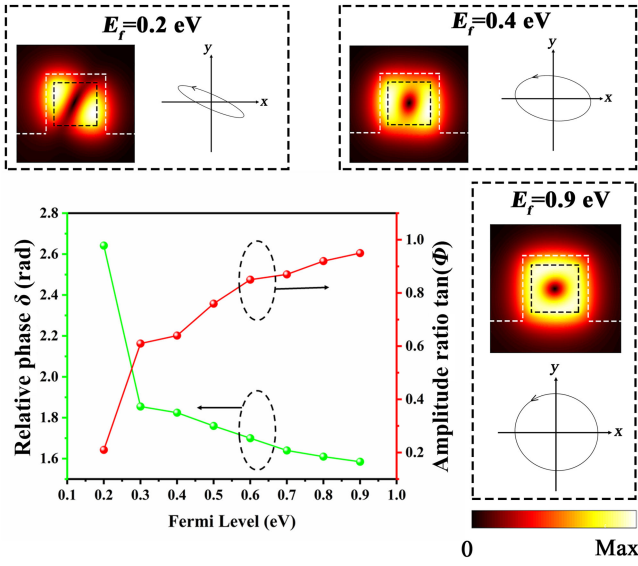
Fig. 7. Curves of relative phase δ and amplitude ratio $\tan(\Phi)$ when the Fermi level changes from 0.2 eV to 0.9 eV, and drawings showing the field distribution of longitudinal component E_Z and the polarization state of transverse component E_T of $E_f = 0.2, 0.4, 0.9$ eV, with $\lambda = 100\ \mu m$, $L_g = 145\ \mu m$ and $\alpha = 45°$.
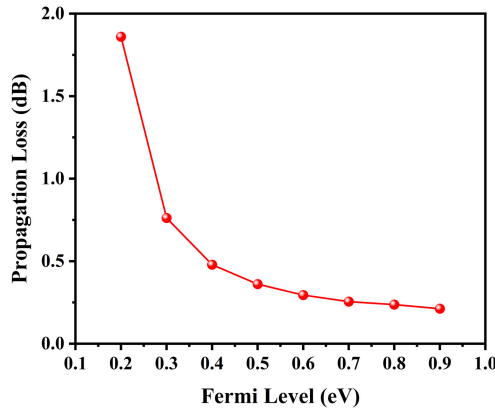

Fig. 8. The dependence of the propagation loss of the graphene hybrid plasmonic waveguide on the graphene Fermi level.

level. When the Fermi level drops from 0.9 eV to 0.2 eV, the propagation loss rises from 0.18 dB to 1.86 dB. The lower the Fermi level, the faster the loss increases. Thus, we can easily control the polarization state of E_T and the field distribution of E_Z by changing the Fermi level E_f of the graphene and the polarization angle α of the incident light without changing the parameters of the structure.

VIII. CONCLUSION

In summary, we have proposed and numerically demonstrated a graphene hybrid plasmonic waveguide that can generate selective SAM and OAM beams in the terahertz regime. This is mainly achieved by using the strong optical confinement and birefringence effect in the hybrid waveguide to the relative phase between the two orthogonal modes. In addition, we use the

concept of birefringence to construct chiral converter and chiral discriminator, which will extend the application of this hybrid waveguide, such as integrated quantum computing, on-chip biosensing, Terahertz communication technology, etc. Finally, based on the dynamic tunable characteristics of graphene, we have realized the dynamic adjustment of the polarization state and the OAM field distribution of the output beams by changing the graphene Fermi level, which will greatly expand the application potential.

REFERENCES

[1] Y. F. Chau, Y. J. Lin, and D. P. Tsai, "Enhanced surface plasmon resonance based on the silver nanoshells connected by the nanobars," *Opt. Express*, vol. 18, no. 4, pp. 3510–3518, Feb. 2010.

[2] C. C. Hu, Y. T. Tsai, W. Yang, and Y. F. Chau, "Effective coupling of incident light through an air region into an S-shape plasmonic Ag nanowire waveguide with relatively long propagation length," *Plasmonics*, vol. 9, no. 3, pp. 573–579, Jan. 2014.

[3] L. Shen, T. J. Yang, and Y. F. Chau, "50/50 beam splitter using a one-dimensional metal photonic crystal with parabolalike dispersion," *Appl. Phys. Lett.*, vol. 90, no. 25, pp. 251909–251909-3, Jul. 2007.

[4] X. S. Lin and X. G. Huang, "Tooth-shaped plasmonic waveguide filters with nanometeric sizes," *Opt. Lett.*, vol. 33, no. 23, pp. 2874–2876, Jan. 2009.

[5] N. F. Chao *et al.*, "Variable optical attenuator and modulator based on a graphene plasmonic gap waveguide," *Opt. Commun.*, vol. 426, pp. 251–256, Mar. 2018.

[6] R. A. Beth, "Mechanical detection and measurement of the angular momentum of light," *Phys. Rev.*, vol. 50, no. 2, pp. 115–125, Jul. 1936.

[7] R. Fickler *et al.*, "Quantum entanglement of high angular momenta," *Science*, vol. 338, no. 6107, pp. 640–643, Nov. 2012.

[8] K. Y. Bliokh, D. Smirnova, and F. Nori, "Quantum spin Hall effect of light," *Science*, vol. 348, no. 6242, pp. 1448–1451, Jun. 2015.

[9] R. Farshchi, M. Ramsteiner, J. Herfort, A. Tahraoui, and H. T. Grahn, "Optical communication of spin information between light emitting diodes," *Appl. Phys. Lett.*, vol. 98, no. 16, Apr. 2011, Paper 162508.

[10] H. Huang *et al.*, "100 Tbit/s free-space data link enabled by three-dimensional multiplexing of orbital angular momentum, polarization, and wavelength," *Opt. Lett.*, vol. 39, no. 2, pp. 197–200, Jan. 2014.

[11] F. Zhang *et al.*, "On chip chirality-distinguishing beamsplitter," *Opt. Express*, vol. 25, no. 21, pp. 24861–24871, Oct. 2017.

[12] M. Khorasaninejad *et al.*, "Multispectral chiral imaging with a metalens," *Nano Lett.*, vol. 16, no. 7, pp. 4595–4600, Jun. 2016.

[13] B. Jack *et al.*, "Holographic ghost imaging and the violation of a bell inequality," *Phys. Rev. Lett.*, vol. 103, no. 8, Aug. 2009, Art. no. 083602.

[14] A. Mair, A. Vaziri, G. Weihs, and A. Zeilinger, "Entanglement of the orbital angular momentum states of photons," *Nature*, vol. 412, no. 6844, pp. 313–316, Jul. 2001.

[15] E. Karimi, S. A. Schulz, I. De Leon, H. Qassim, J. Upham, and R. W. Boyd, "Generating optical orbital angular momentum at visible wavelengths using a plasmonic metasurface," *Light Sci. Appl.*, vol. 3, no. 5, p. e167, May 2014.

[16] N. Bozinovic *et al.*, "Terabit-scale orbital angular momentum mode division multiplexing in fibers," *Science*, vol. 340, no. 6140, pp. 1545–1548, Jun. 2013.

[17] S. Zheng and J. Wang, "On-chip orbital angular momentum modes generator and (de)multiplexer based on trench silicon waveguides," *Opt. Express*, vol. 25, no. 15, pp. 18492–18501, Jul. 2017.

[18] D. S. Ding *et al.*, "Quantum storage of orbital angular momentum entanglement in an atomic ensemble," *Phys. Rev. Lett.*, vol. 114, no. 5, Feb. 2015, Art. no. 050502.

[19] I. V. Goltser *et al.*, "An adjustable quarter-wave plate," *Opt. Commun.*, vol. 97, no. 5–6, pp. 291–294, Apr. 1993.

[20] Y. F. Chau, H. H. Yeh, and D. P. Tsai, "Significantly enhanced birefringence of photonic crystal fiber using rotational binary unit cell in fiber cladding," *Jpn. J. Appl. Phys.*, vol. 46, no. 43, pp. L1048–L1051, Nov. 2007.

[21] Y. S. Sun, Y. F. Chau, H. H. Yeh, and D. P. Tsai, "Highly birefringent index-guiding photonic crystal fiber with squeezed differently sized air-holes in cladding," *Jpn. J. Appl. Phys.*, vol. 47, no. 5, pp. 3755–3759, May 2008.

[22] Y. F. Chau, C. Y. Liu, H. H. Yeh, and D. P. Tsai, "A comparative study of high birefringence and low confinement loss photonic crystal fiber employing elliptical air holes in fiber cladding with tetragonal lattice," *Prog. Electromagn. Res. B*, vol. 22, no. 1, pp. 39–52, Jan. 2010.

[23] K. Y. Yang, Y. F. Chau, Y. W. Huang, H. Y. Yeh, and D. P. Tsai, "Design of high birefringence and low confinement loss photonic crystal fibers with five rings hexagonal and octagonal symmetry air-holes in fiber cladding," *J. Appl. Phys.*, vol. 209, no. 9, pp. 093103–093103-5, May 2011.

[24] C. J. Min *et al.*, "Focused plasmonic trapping of metallic particles," *Nature Commun.*, vol. 4, no. 2891, pp. 1–7, Dec. 2013.

[25] Y. Zhao and A. Alù, "Manipulating light polarization with ultrathin plasmonic metasurfaces," *Phys. Rev. B*, vol. 84, no. 20, Nov. 2011, Art. no. 205428.

[26] B. Yang, W. M. Ye, X. D. Yuan, Z. H. Zhu, and C. Zeng, "Design of ultrathin plasmonic quarter-wave plate based on period coupling," *Opt. Lett.*, vol. 38, no. 5, pp. 679–681, Mar. 2013.

[27] T. Guo and C. Argyropoulos, "Broadband polarizers based on graphene metasurfaces," *Opt. Lett.*, vol. 41, no. 23, pp. 5592–5595, Nov. 2016.

[28] J. Guo, Y. Liang, X. G. Huang, B. Guo, and J. Li, "Pure dielectric waveguides enable compact, ultrabroadband wave plates," *IEEE Photon. J.*, vol. 8, no. 5, pp. 1–9, Oct. 2016.

[29] D. G. Grier, "A revolution in optical manipulation," *Nature*, vol. 424, no. 6950, pp. 810–816, Aug. 2003.

[30] M. W. Beijersbergen *et al.*, "Helical-wavefront laser beams produced with a spiral phase plate," *Opt. Commun.*, vol. 112, no. 5–6, pp. 321–327, Dec.1994.

[31] J. Courtial and J. M. Padgett, "Performance of a cylindrical lens mode converter for producing Laguerre–Gaussian laser modes," *Opt. Commun.*, vol. 159, no. 1–3, pp. 13–18, Jan. 1999.

[32] S. Slussarenko, A. Murauski, T. Du, V. Chigrinov, L. Marrucci, and E. Santamato, "Tunable liquid crystal q-plates with arbitrary topological charge," *Opt. Express*, vol. 19, no. 5, pp. 4085–4090, Feb. 2011.

[33] X. L. Wang *et al.*, "Quantum teleportation of multiple degrees of freedom of a single photon," *Nature*, vol. 518, no. 7540, pp. 516–519, Feb. 2015.

[34] M. Verma, S. K. Pal, A. Jejusaria, and P. Senthilkumaran, "Separation of spin and orbital angular momentum states from cylindrical vector beams," *Optik*, vol. 132, pp. 121–126, Mar. 2017.

[35] X. Ma, C. H. Liu, G. Chang, and A. Galvanauskas, "Angular-momentum coupled optical waves in chirally-coupled-core fibers," *Opt. Express*, vol. 19, no. 27, pp. 26515–26528, Dec. 2011.

[36] Y. Jiang, G. Ren, W. Jin, Y. Xu, W. Jian, and S. Jian, "Polarization properties of fiber-based orbital angular momentum modes," *Opt. Fiber Technol.*, vol. 38, pp. 113–118, Nov. 2017.

[37] G. Li *et al.*, "Nonlinear metasurface for simultaneous control of spin and orbital angular momentum in second harmonic generation," *Nano Lett.*, vol. 17, no. 12, pp. 7974–7979, Nov. 2017.

[38] Q. Tan, Q. Guo, H. Liu, X. G. Huang, and S. Zhang, "Controlling plasmonic orbital angular momentum by combining geometric and dynamic phases," *Nanoscale*, vol. 9, no. 15, pp. 4944–4949, Apr. 2016.

[39] Y. Liang, H. W. Wu, B. J. Huang, and X. G. Huang, "Light beams with selective angular momentum generated by hybrid plasmonic waveguides," *Nanoscale*, vol. 6, no. 21, pp. 12360–12365, Aug. 2014.

[40] Y. Liang, F. Zhang, J. Gu, X. G. Huang, and S. Liu, "Integratable quarter-wave plates enable one-way angular momentum conversion," *Sci. Rep.*, vol. 6, no. 1, Apr. 2016, Paper 24959.

[41] C. D. Nordquist, M. C. Wanke, A. M. Rowen, C. L. Arrington, A. D. Grine, and C. T. Fuller, "Properties of surface metal micromachined rectangular waveguide operating near 3 THz," *IEEE J. Sel. Topics Quantum Electron.*, vol. 17, no. 1, pp. 130–137, Jun. 2010.

[42] C. Wu, S. Khanal, J. L. Reno, and S. Kumar, "Terahertz plasmonic laser radiating in an ultra-narrow beam," *Optica*, vol. 3, no. 7, pp. 734–740, Jul. 2016.

[43] X. He *et al.*, "Ultralow loss graphene-based hybrid plasmonic waveguide with deep-subwavelength confinement," *Opt. Express*, vol. 26, no. 8, pp. 10109–10118, Apr. 2018.

[44] A. H. C. Neto, F. Guinea, N. M. R. Peres, K. S. Novoselov, and A. K. Geim, "The electronic properties of graphene," *Rev. Mod. Phys.*, vol. 81, no. 1, p. 109, Jan. 2009.

[45] A. Vakil and N. Engheta, "Transformation optics using graphene," *Science*, vol. 332, no. 6035, pp. 1291–1294, Jun. 2011.

[46] F. H. L. Koppens, D. E. Chang, and F. J. Garcia de Abajo, "Graphene plasmonics: A platform for strong light–matter interactions," *Nano Lett.*, vol. 11, no. 8, pp. 3370–3377, Jul. 2011.

[47] L. Ju *et al.*, "Graphene plasmonics for tunable terahertz metamaterials," *Nat. Nanotechnol.*, vol. 6, no. 10, pp. 630–634, Sep. 2011.

[48] K. F. Mak, M. Y. Sfeir, Y. Wu, C. H. Lui, J. A. Misewich, and T. F. Heinz, "Measurement of the optical conductivity of graphene," *Phys. Rev. Lett.*, vol. 101, no. 19, Nov. 2008, Art. no. 196405.

[49] T. Jin, W. Lin, and G. Zheng, "Graphene surface-polariton in-plane Cherenkov radiation," *Carbon*, vol. 133, pp. 249–253, Mar. 2018.

[50] C. H. Gan, "Analysis of surface plasmon excitation at terahertz frequencies with highly doped graphene sheets via attenuated total reflection," *Appl. Phys. Lett.*, vol. 101, no. 11, p. 111609, Sep. 2012.

[51] P. Y. Chen and A. Alu, "Atomically thin surface cloak using graphene monolayers," *ACS Nano*, vol. 5, no. 7, pp. 5855–5863, Jun. 2011.

[52] D. K. Efetov and P. Kim, "Controlling electron–phonon interactions in graphene at ultrahigh carrier densities," *Phys. Rev. Lett.*, vol. 105, no. 25, Dec. 2010, Art. no. 256805.

[53] C. Casiraghi *et al.*, "Rayleigh imaging of graphene and graphene layers," *Nano Lett.*, vol. 7, no. 9, pp. 2711–2717, Aug. 2007.

[54] A. Taflove and S. C. Hagness, "*Computational Electrodynamics: The Finite-Difference Time-Domain Method*," 2nd ed. Boston, MA, USA: Artech House, 2000.

[55] Lumerical FDTD Solutions, Lumerical, Mar. 2013. [Online]. Available: http://www.lumerical.com/tcad-products/fdtd/

[56] K. L. Vodopyanov and Y. H. Avetisyan, "Optical terahertz wave generation in a planar GaAs waveguide," *Opt. Lett.*, vol. 33, no. 20, pp. 2314–2316, Oct. 2008.

[57] S. Atakaramians, S. Afshar, T. M. Monro, and D. Abbott, "Terahertz dielectric waveguides," *Adv. Opt. Photon.*, vol. 5, no. 2, pp. 169–215, Jul. 2013.

[58] A. Y. Cho and J. R. Arthur, "Molecular beam epitaxy," *Prog. Solid-State Chem.*, vol. 10, pp. 157–191, 1975.

[59] R. Cheung, S. Thoms, S. P. Beamont, G. Doughty, V. Law, and C. D. W. Wilkinson, "Reactive ion etching of GaAs using a mixture of methane and hydrogen," *Electron. Lett.*, vol. 23, no. 16, pp. 857–859, Jul. 1987.

[60] J. B. Driscoll, X. Liu, S. Yasseri, I. Hsieh, J. I. Dadap, and R. M. Osgood, "Large longitudinal electric fields (Ez) in silicon nanowire waveguides," *Opt. Express*, vol. 17, no. 4, pp. 2797–2804, Feb. 2009.

[61] M. Z. Alam, J. N. Caspers, J. S. Aitchison, and M. Mojahedi, "Compact low loss and broadband hybrid plasmonic directional coupler," *Opt. Express*, vol. 21, no. 13, pp. 16029–16034, Jul. 2013.